Hypersonic Turbulent Boundary-Layer Density Fluctuations: Direct Numerical Simulation, Focused Laser Differential Interferometry

Ahsan Hameed,* Ben Segall,† Jaden Kokinakos,† and Nick J. Parziale‡
Stevens Institute of Technology, Hoboken, New Jersey 07030
and
Dhiman Roy§ and Lian Duan¶
The Ohio State University, Columbus, Ohio 43210

https://doi.org/10.2514/1.J067009

In this article, we present a comparison of experimental measurements of density fluctuations over a hollow cylinder to direct numerical simulation (DNS) data at similar conditions and wall-normal positions. The experimental observations are made using a closely spaced multiple-beam-pair focused laser differential interferometry (FLDI) flow diagnostic, allowing data to be acquired above 1 MHz. The power spectral density (PSD), autocorrelation and cross-correlation, and coherence spectra computed from FLDI and DNS data are presented for comparison. The PSD spectra obtained from experimental results and numerical analysis show good agreement in the energy-containing and inertial subrange, with a minor deviation in the higher frequencies of the dissipation range. A comparison of the cross-correlation maintains the agreement in the energy-containing and inertial ranges, but shows slightly higher correlation values for DNS data until it asymptotically approaches zero. The coherence spectra consistently show that the DNS data remain better correlated at higher frequencies. However, both datasets show steep reductions in correlation with increasing probe separation distances, extending into the lower frequencies of the energy-containing and inertial ranges.

I. Introduction

A THOROUGH understanding of turbulent boundary layers at hypersonic Mach numbers is important to the design of high-speed vehicles. Turbulent boundary layers dramatically increase the aerodynamic drag and heating rate over the vehicle's surface. In tests of ballistic reentry vehicles, the surface heating rate was found to increase by a factor of 5 within the turbulent boundary layer [1]. For slender bodies, the heating rate was found to have increased by a factor of 3 following transition to turbulence [2,3]. Furthermore, fluctuations in pressure within the turbulent boundary layer can induce vibrational loading on aerodynamic surfaces and impact the structural integrity of the high-speed vehicle [4,5].

To provide a comprehensive representation of a turbulent boundary layer, experimental diagnostic techniques and computational simulation methods must be able to resolve disturbances of frequencies that span the entirety of the energy cascade, from the large energy-containing structures to the small dissipative eddies. Experimentalists have found focused laser differential interferometry (FLDI) to be an appropriate flow diagnostic for turbulence studies because of its excellent spatial resolution (<100 μm) perpendicular to the beam propagation axis, large frequency bandwidth (10 kHz to 10 MHz), and high sensitivity at low densities (0.1 g/m^3) [6]. Developed by Smeets [7–12] and Smeets and George [13] in the 1970s, FLDI is a common-path polarizing interferometer sensitive to the phase difference between the interfering beam pairs. In 2012, Parziale et al. [14–20] advanced the FLDI technique and used it to characterize the facility disturbance level and boundary-layer instability and transition in the Caltech T5 reflected-shock tunnel. Researchers have recently used the technique to make reliable measurements of convective velocity between two closely spaced FLDI prove volumes [6,21–27], facility disturbance-level characterization [28–30] and have developed beam-shaping techniques for application of the technique in hard-to-access flows [31–35]. Researchers have used controlled problems [36–38] to test the data-reduction strategies developed by Fulghum [39], Settles and Fulghum [40], Schmidt and Shepherd [41], and Hameed and Parziale [42].

Experimental investigations of hypersonic turbulent boundary layers have historically been made with diagnostic techniques such as hot-wire anemometry, which have been limited by poor frequency or particle response and spatial resolution [43]. Measurements of pressure fluctuations within high-speed turbulent boundary layers have been limited to the surface and have suffered from significant scatter in magnitude [44,45] and from poor spatial resolution and frequency response [46]. Recently, optical diagnostic techniques have been implemented to study hypersonic turbulent boundary layers. Camillo et al. [47] employed a multipoint FLDI setup to probe the hypersonic turbulent boundary layer over a 7° half-angle cone at several heights above the model surface. They found the convective velocity of density disturbances agreed with similar measurements of pressure disturbances, and the density spectra showed evidence of power-law scaling previously observed in the pressure spectra. Benitez et al. [48] used direct numerical simulation (DNS) to model the behavior of a computational FLDI passing through a hypersonic turbulent boundary layer. They found that integration along the optical axis resulted in lower FLDI amplitudes than for true point measurements and determined that the finite spacing between the FLDI beams resulted in amplitude roll-off at low-frequencies.

High-speed turbulent boundary layers have also been investigated using DNS, which requires high spatiotemporal resolution to capture the vast scales of turbulence. Regarding inflow generation

Presented as Paper 2024-2734 at the AIAA Scitech 2024 Forum, Orlando, FL, January 8–12, 2024; received 19 February 2026; accepted for publication 27 May 2026; published online 3 September 2026.

*Research Engineer, Mechanical Engineering, 1 Castle Point on Hudson; ahsanhameed@gmail.com (Corresponding Author).

†Graduate Student, Mechanical Engineering, 1 Castle Point on Hudson.

‡George Meade Bond Professor, Mechanical Engineering, 1 Castle Point on Hudson. Associate Fellow AIAA.

§Graduate Research Associate, Departments of Mechanical & Aerospace Engineering. Student Member AIAA.

¶Professor, Department of Mechanical & Aerospace Engineering. Associate Fellow AIAA.

techniques, significant emphasis has been placed on using long streamwise domains to ensure that the flow reaches fully developed equilibrium turbulence and that turbulent structures are sufficiently decorrelated prior to the analysis plane [49–54]. Notably, Martin [55] developed a local initialization procedure for supersonic and hypersonic flows that produced controlled conditions over a wide range of Reynolds and Mach numbers. The results showed good agreement with experimental data regarding turbulent shear stresses and fluctuations in velocity and temperature.

Leveraging these high-fidelity simulation frameworks, Pirozzoli and Bernardini [50] performed a large-scale DNS simulation to study a turbulent boundary layer at supersonic flow ($M_\infty = 2$) and $Re_\tau = 1120$, and found excellent agreement of velocity statistics compared to incompressible data with the application of appropriate scaling factors. Duan et al. [56] performed a DNS study of turbulent boundary layers at Mach 5 to assess the influence of wall temperature on turbulence relations and compressibility effects and found that the scaling relations used to express adiabatic compressible boundary-layer statistics in terms of incompressible boundary layers also held for nonadiabatic cases. They extended the analysis to study the effect of Mach number [57] and high enthalpy [58], finding that many of the scaling relations derived based on the weak compressibility hypothesis remain valid for high Mach numbers and enthalpy. Duan et al. [59] used DNS to study the pressure fluctuations generated within a turbulent boundary layer at different wall-normal locations over a flat plate. They found that the dominant frequency of boundary-layer-induced pressure fluctuations shifted to lower frequencies as the location of interest moved away from the wall. Furthermore, they showed good agreement between DNS and experimental data and the expected power-law scaling in regions of low, mid, and mid-to-high overlap and acceptable agreement at high frequencies. Recent work has extended the numerical analysis of turbulent boundary layers to higher Mach numbers ($M_\infty = 11$ and 14) with strong wall-cooling ($T_w/T_R \approx 0.2$) [60]. Additionally, Zhang et al. [61] presented a DNS database for high-speed, zero-pressure-gradient turbulent boundary layers over a wide range of nominal freestream Mach numbers ($M_\infty = 2.5$–14) and wall-to-recovery temperature ratios ($T_w/T_R = 0.18$–1.0) at appreciable Reynolds numbers ($Re_\tau = 450$–646) to gauge the performance of compressibility transformations in the high-Mach-number, cold-wall regime, finding good success applying various compressibility transformations in most of the boundary layer. Huang et al. [54] extended this analysis to $Re_\tau \leq 1200$ to confirm the validity of compressibility transformations at moderately high Reynolds numbers.

In this work, we study the turbulent boundary layer generated over a hollow cylinder using a multibeam-pair FLDI diagnostic [62,63]. The experimental measurements of the density fluctuations obtained by FLDI are compared to a DNS solution produced using the experimental flow conditions and model geometry. We compare the DNS and FLDI spectra with the expected power-law scalings in their respective ranges. The closely spaced FLDI beams used to probe the boundary layer enabled density disturbance measurements well into the dissipation range of the turbulence spectra. Furthermore, we present a comparison of the auto- and cross-correlations between experimentally measured and computationally simulated density fluctuations. These results highlight the variation in experimental and computational agreement across the relevant frequency scales. Finally, the coherence spectra for experimentally measured and computationally simulated density fluctuations are presented at increasing spatial separations to demonstrate spectral attenuation within the aforementioned scaling ranges.

II. Facility and Experimental Setup

All experiments in this work were conducted at the Stevens Shock Tunnel (SST) at Stevens Institute of Technology. The SST is a reflected shock tunnel capable of replicating Mach 6 free-flight flow conditions at an enthalpy of 1.5 MJ/kg. The facility can produce unit Reynolds numbers of $0.35 - 8.1 \times 10^6\ \mathrm{m}^{-1}$ for at least 4 ms [64]; higher Reynolds numbers can be achieved at reduced enthalpy, or "cold flow" conditions. A schematic of the facility is shown in Fig. 1.

The facility was operated in a fashion similar to other shock tunnels. The driver and driven sections were separated by a double-diaphragm section, which allowed the driver pressure to be prescribed depending on the diaphragm thickness and provided an accurate, controlled, and repeatable test method. Aluminum 1100 diaphragms were used, with their thickness dependent on the shot conditions. A thinner aluminum diaphragm was used to separate the driven section from the nozzle, test section, and dump tanks. Following the installation of the diaphragms, the entire facility was evacuated to an acceptable level of vacuum, with the test section reaching approximately 33 Pa. Next, the driven section was filled with the test gas to the tailored run condition, and the driver and double-diaphragm sections were filled with the driver gas. For this experiment, the driver section was filled with pure N_2, and the driven gas was a 5% Kr/95% N_2 mixture. During the filling process, the pressure in the double-diaphragm station was maintained at approximately half the driver pressure. The experiment started once the gas in the double-diaphragm section was rapidly evacuated.

The reservoir conditions were determined using Cantera [65] with the Shock and Detonation Toolbox [66], taking into account the pressure of the driven tube, P_1, and the measured incident shock speed, U_s. The relevant conditions for the experiment analyzed in this work (shot 385) are shown in Table 1. Here, boundary-layer quantities such as the boundary-layer thickness (δ), viscous length (y_τ), and friction velocity (u_τ) were determined as described in Segall et al. [67]. The model, shown in Fig. 2, used in these experiments was a 1-m-long hollow-cylinder flare (HCF). The model featured a 5° removable nose tip with a sharp leading edge, a 0.102-m-outer-diameter hollow cylinder, and a 34° flare of maximum diameter 0.203 m. Strips of roughness elements (sandpaper) were placed near the leading edge of the model to artificially trip the boundary layer and promote transition to turbulence.

FLDI was used as the flow diagnostic for the experiments presented in this work. The FLDI beams were positioned within the turbulent boundary layer, approximately 0.7 m from the model's leading edge and at approximately 6.7 mm above the surface of the hollow cylinder. As shown in Fig. 3a, the beam pairs were oriented in a single row of six columns, with each column interspaced by

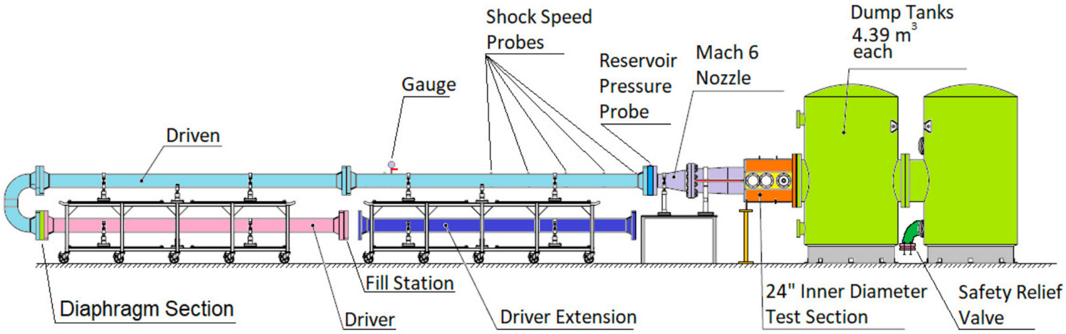

Fig. 1 Schematic of the Stevens Shock Tunnel identifying the driver and driven sections, Mach 6 nozzle, 24-inch test section, and dump tanks.

Table 1 Experimental conditions for FLDI shot 385 performed at the Stevens Shock Tunnel (boundary-layer properties estimated using DNS)

Parameter	Value
Shot	385
δ, mm	10
U_e, m/s	942
T_w, K	295
T_r, K	533
T_w/T_r	0.54
T_∞, K	65.3
Re^U_∞, 1/m	14×10^6
M_∞	6.32
Re_θ	5293
y_τ, m	2.6e–05
u_τ, m/s	48
Re_τ	370

approximately 2.4 mm. A magnified view of a single FLDI beam pair is shown in Fig. 3b, showing a beam intraspacing of approximately 0.04 mm.

The components used to generate the closely spaced multiple-beam-pair FLDI diagnostic are shown in Fig. 3c. In this setup, the diffractive optical element was used to generate a single row of 6 beam pairs, and its placement and specification prescribed the beam interspacing seen in Fig. 3a. A Wollaston prism of 1 arcminute was used to generate the streamwise beam intraspacing. Downbeam of the test section, a complementary 1-arcminute Wollaston prism was used to recombine the intraspaced beams. Each of the six recombined beams was focused on individual photodetectors, which registered a voltage change as a result of the interference caused by the differing optical path lengths traversed by the individual beams within the beam pair. The close interspacing within each row of beams required the use of an array of converging and diverging lenses (not pictured) to separate the recombined beams by a practical distance. Additional converging lenses were used to focus each beam onto its respective photodiode.

III. DNS Solutions

As noted in the Introduction, a DNS was performed on the hollow-cylinder (HC) section of the hollow-cylinder-flare (HCF) test article to enable comparison with the FLDI. This section details the simulation setup for the HC DNS. The DNS provides fully resolved space–time density fields, which serve as a reference for interpreting the FLDI data. Single- and multipoint density statistics from the DNS—including power spectral density, auto- and cross-correlations, and spatial coherence—are directly compared with the FLDI measurements in later sections to cross-validate experiment and simulation and to analyze the spectral and structural characteristics of density fluctuations in a hypersonic turbulent boundary layer.

A. Flow Conditions and Computational Domain

Table 2 summarizes the freestream and wall-temperature conditions used for the HC DNS. The DNS is conducted for the turbulent boundary layer over the HCF model at a nominal Mach number of 6.32, and the wall temperature is fixed at $T_w = 295$ K, which corresponds to a wall-to-recovery temperature ratio of $T_w/T_r = 0.54$ with a recovery factor $r = 0.89$. The freestream and wall temperature conditions of the DNS closely match the operating conditions of the experiment in the Stevens Shock Tunnel.

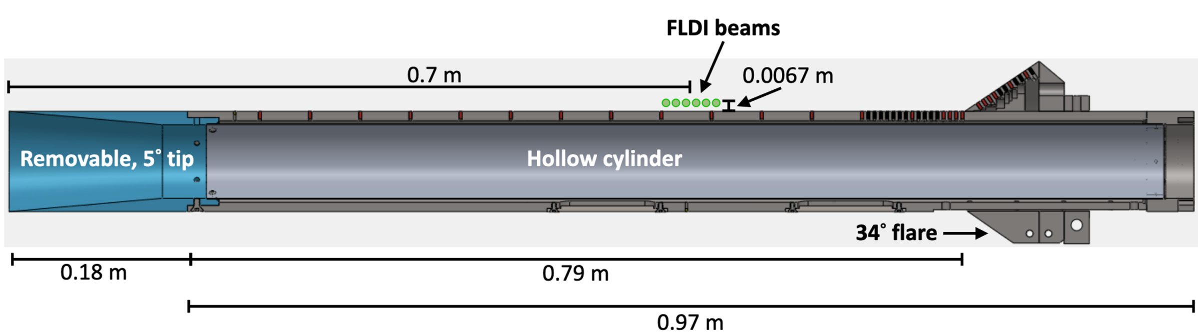

Fig. 2 Section view of HCF showing removable 5° tip, hollow cylinder, 34° flare, and location of FLDI beams.

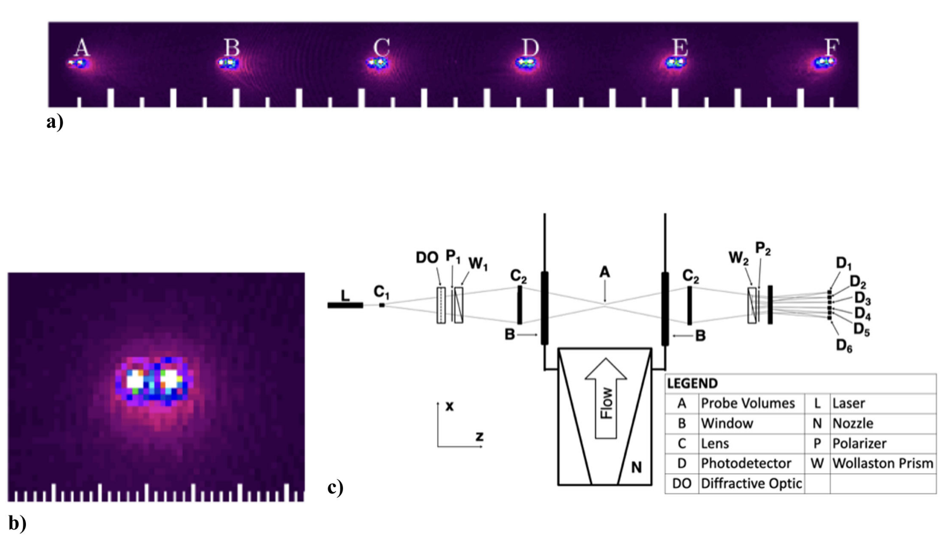

Fig. 3 a) Picture of FLDI beams (major/minor ticks at 1 mm/0.5 mm). b) Close-up of individual FLDI beam pair (major/minor ticks at 0.50 mm/0.10 mm). c) Components for FLDI setup.

Table 2 Freestream conditions and wall temperatures for the HC DNS case

Parameter	Value
M_∞	6.32
Re_∞, 1/m	13.6×10^6
U_∞, m/s	992.4
ρ_∞, kg/m^3	0.063
T_∞, K	65.25
T_w, K	295.0

To initialize the DNS and establish the necessary inflow conditions, a precursor RANS simulation was first performed using ANSYS Fluent [68]. This RANS calculation covers the entire HCF model geometry, capturing the nose-tip physics and the development of the leading-edge shock. The DNS domain, illustrated in Fig. 4, is strategically positioned to begin at $x = 0.305$ m ($x/L \approx 0.316$). This location is selected to align with the experimental setup, where a sandpaper trip is used to force boundary-layer transition. By placing the DNS inflow slightly downstream of the physical trip location, the simulation can bypass the complex transition region and immediately establish a fully developed turbulent state using synthetic turbulence generation. As shown in the top panel of Fig. 4, the top boundary of the DNS domain is placed entirely beneath the leading-edge shock captured by the RANS.

A single DNS domain with an azimuthal extent of $\phi = 60°$ is employed, spanning the axial range from $x/L = 0.316$ to 0.931, where L is the cylinder length. At the inlet of the DNS domain, the boundary-layer thickness is $\delta_i = 4.9$ mm and the streamwise length of the domain is $L_x = 123\delta_i$. Uniform grids are used in the streamwise and azimuthal directions with $\Delta x^+ = 4.73$ and $(r\Delta\theta)^+_w = 2.65$. The wall-normal grids are refined near the wall with $\Delta y^+_w = 0.47$, gradually stretching to $\Delta y^+_\delta = 3.71$ near the boundary-layer edge. Detailed grid parameters are presented in Table 3. The chosen azimuthal domain $\phi = 60°$ yields a

Table 3 Grid resolution and domain size for the HC DNS (normalizations are done using the values indicated in Table 4)

Parameter	Value
x_{beg}, m	0.305
x_{end}, m	0.898
ϕ, deg	60
$N_x \times N_\phi \times N_r$	$4700 \times 750 \times 750$
Δx^+	4.73
$(r\Delta\phi)^+_w$	2.65
$(r\Delta\phi)^+_\delta$	3.24
Δy^+_w	0.47
Δy^+_δ	3.71
$T_f u_\tau/\delta$	5.8

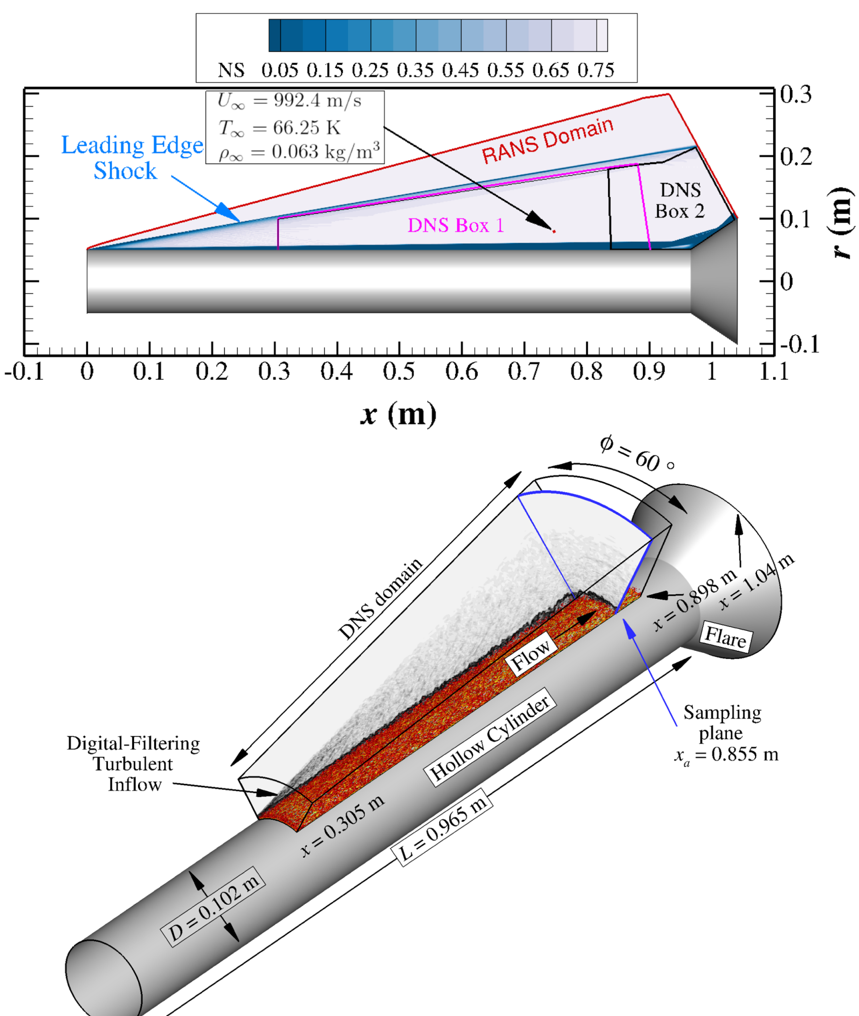

Fig. 4 Computational domain and simulation setup for the present DNS case. Top: DNS domain along with precursor RANS. Bottom: instantaneous isosurface of normalized density gradient.

spanwise-equivalent domain $L_y/\delta \approx 4.74$ at the sampling location, which allows sufficient decay of spanwise correlations and avoids azimuthal locking of large-scale structures.

B. Numerical Method and Boundary Conditions

The simulations solve the three-dimensional compressible Navier–Stokes equations in conservative form using cylindrical coordinates. In the HC DNS, the working fluid is modeled as a calorically perfect gas with a molecular mass of $M = 30.803$ kg/kmol and a specific heat ratio of $\gamma = 1.4077$, providing an approximation of the nitrogen–krypton mixture used in the experiment. The dynamic viscosity is determined via Keyes' law [69], while the thermal conductivity κ is computed assuming a constant molecular Prandtl number of $Pr = 0.71$ such that $\kappa = \mu c_p/Pr$.

The inviscid fluxes are discretized using a seventh-order Weighted Essentially Non-Oscillatory (WENO) scheme, which is optimized by adjusting the frequency of WENO adaptations. A fourth-order central difference technique is used to discretize the viscous fluxes, while a third-order low-storage Runge–Kutta scheme is employed for time integration, ensuring accurate and efficient computations. At the inflow, turbulent fluctuations are prescribed using the modified digital-filter method for nonuniform curvilinear grids of Dhamankar et al. [70]. To ensure that the DNS accurately represents the experimental turbulent state, the mean velocity field and the turbulent shear stress terms required for the digital-filter method are extracted directly from the converged precursor RANS solution at the $x = 0.305$ m station. Digitally filtered random disturbances are superimposed on the prescribed mean inflow profiles to promote immediate turbulent content and bypass transition. The detailed inflow methodology and numerical setup are provided in Roy et al. [71]. The top boundary utilizes an unsteady, nonreflecting boundary condition. A periodic boundary condition is applied in the azimuthal direction. At the wall, a no-slip, isothermal wall condition is imposed. Grid sensitivity on the spectral content for the present HC DNS is assessed in the Appendix, while the corresponding first- and second-order turbulent statistics and their grid independence for the same geometry and methodology are reported in Roy et al. [71].

C. Statistical Sampling and Analysis Locations

Flow statistics, power spectral densities (PSDs), spectral coherence, and related quantities are evaluated at selected downstream sampling planes where the boundary layer is fully developed and sufficiently upstream of the flare-induced shock–boundary-layer interaction and separation region. Boundary-layer properties and viscous scaling parameters at these sampling locations are summarized in Table 4. The density spectra are obtained from planar density records sampled at 16.67 MHz and at different wall-normal heights. Each signal is detrended and preconditioned with a Hanning window. The total signal is divided into eight 50% overlapping segments. Spectral estimates are computed using Welch's method and subsequently averaged across all azimuthal planes to suppress statistical variability. Correlation coefficients and coherence spectra were computed at the same DNS sampling location and similarly ensemble-averaged across the azimuthal plane within $\phi = \pm 30°$ of the hollow cylinder's top dead center. The total data-collection time used for spectral estimation is $T_f u_\tau \delta = 5.8$. The chosen sampling durations are sufficient to ensure convergence of the low-frequency content of the PSDs and to support statistically robust estimates of spectral coherence presented in Sec. IV.

Table 4 Boundary-layer properties at the DNS sampling location along the hollow cylinder, $x_a = 0.855$ m

Parameter	Value
x_a/D	8.38
Re_θ	6084
Re_τ	421
$Re_{\delta 2}$	1582
θ, mm	0.45
H	14.66
δ, mm	11.26
y_τ, μm	26.77
u_τ, m/s	47.55

IV. Results

In this section, we present comparisons between the experimental results obtained at the Stevens Shock Tunnel and the DNS computations. Specifically, the power spectral density, correlation in the streamwise direction, and coherence between two points with varying spatial streamwise separation are compared.

A. Spectral Comparison

Figure 5a shows the spectra for phase change computed from data collected by all FLDI detectors as well as the experimental noise floor. The PSD was computed using Welch's method with a Hanning window size of approximately 500,000 samples at 50% overlap to provide 3 kHz of spectral resolution. Each spectrum was divided by the frequency vector to represent the differencing nature of the FLDI instrument. Disregarding the spurious noise spikes seen in the spectra for Detector C, the spectra for all FLDI detectors showed excellent agreement and reached the noise floor at approximately $f = 3.5$ MHz. In addition to the spectral comparison between FLDI detectors for shot 385, we present a spectral comparison between shots for a single FLDI detector in Fig. 5b. We note the excellent agreement of the spectra throughout the relevant frequency range between the three experiments run at the same nominal conditions.

The density fluctuation spectra computed from the experimental and numerical datasets are presented in Fig. 6. In Fig. 6a, the DNS spectra are presented for wall-normal locations in the range of $7.4e^{-4} \leq y/\delta \leq 1$. Two FLDI spectra are overlaid, representing corrections to the FLDI spectra due to the 1) differencing effects of the instrument and 2) the finite width of the disturbance field. On the abscissa, the spectra are normalized to the outer length scale ($\omega\delta/U_\infty$) by the respective boundary-layer thickness and freestream velocity.

In Fig. 6b, the density fluctuation spectrum for the DNS simulation was extracted at $y/\delta = 0.66$ for comparison with experimental results obtained using the FLDI diagnostic. The spectra are presented in the outer and inner length scales, and all spectra are normalized by the area under each respective curve.

The measured time-series phase difference between the FLDI beams was converted to density fluctuation spectra using the process detailed in Hameed and Parziale [42]. Namely, the phase difference between the two signals was related to density using the Gladstone–Dale relation, and the spectral response of the measured density fluctuations of an ideal FLDI instrument was approximated using transfer functions. Two variations of the density fluctuation spectrum were computed for experimental data gathered using the FLDI diagnostic. The spectrum labeled "differencing only" considered an infinitesimally thin sinusoidal disturbance at the focus of the FLDI beams and accounted only for the differencing effects of the instrument, modeled using the transfer function of the form

$$H(\kappa) = \frac{2}{\kappa \Delta x} \sin\left(\frac{\kappa \Delta x}{2}\right) \tag{1}$$

where Δx represents the beam intraspacing. The second FLDI spectrum shown in Fig. 6b incorporates the effect of the FLDI beams propagating through a sinusoidal density disturbance field fluctuating in x and y, confined to the area between the hollow-cylinder flare and the boundary-layer edge, modeled as

$$H(\kappa) = \frac{2\pi^{3/2} w_0}{\kappa^2 \lambda \Delta x L} \sin\left(\frac{\kappa \Delta x}{2}\right) \exp\left(-\frac{w_0^2 \kappa^2}{4}\right) \mathrm{erf}\left[\frac{L\kappa\lambda}{2\pi w_0}\right] \tag{2}$$

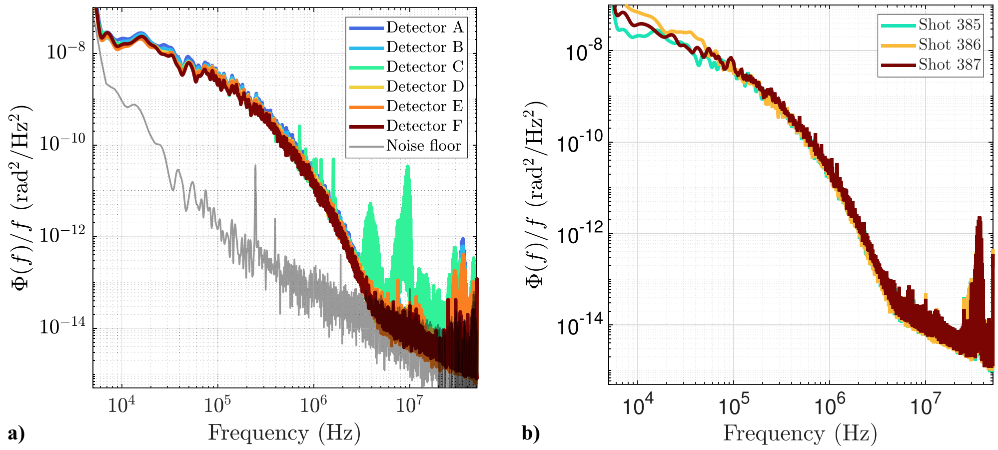

Fig. 5 a) Phase-change spectra for all FLDI detectors, with the diagnostic noise floor shown for reference, and b) a spectral comparison among shots 385, 386, and 387.

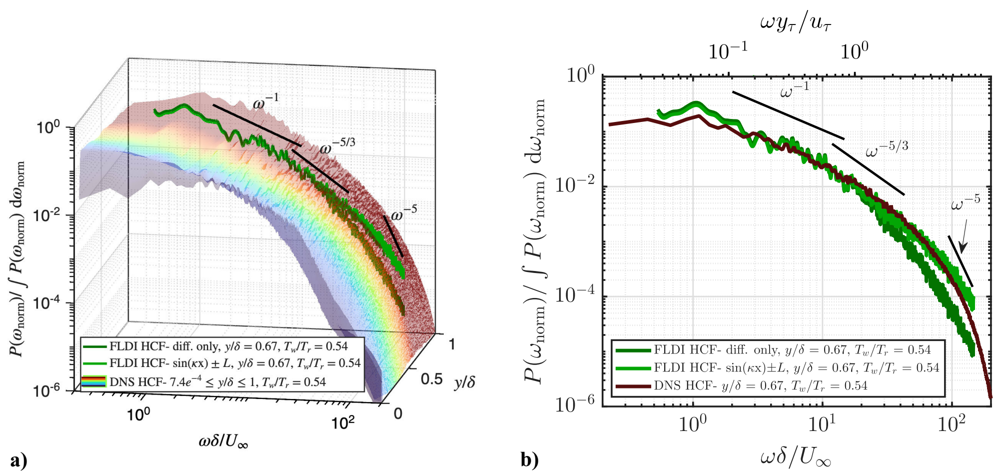

Fig. 6 Normalized FLDI and DNS density fluctuation spectra at a) $7.4e^{-4} \le y/\delta \le 1$ and b) $y/\delta = 0.67$, with power-law scalings for reference.

where w_0 is the beam waist radius, λ is the laser wavelength, and L is the integration length of the FLDI instrument. As shown in Fig. 7, the FLDI beams traverse this region between $-0.02\ \mathrm{m} \le x = L \le 0.02$ m. Additionally, the power-law scalings for the energy-containing range, inertial subrange, and dissipation range are provided as a reference.

Based on the adherence of the DNS HCF spectrum to the expected scaling, the energy-containing range occurs between $2 \le \omega\delta/U_\infty \le 15$ in the outer length scale. All spectra appear to follow the expected ω^{-1} slope in this region and agree with each other. Within the inertial subrange ($12 \le \omega\delta/U_\infty \le 43$), a disparity is observed between the two FLDI spectra. Compared to the spectrum only accounting for the instrument's differencing effects, the FLDI spectrum corrected assuming a density disturbance field of a finite length shows an extended region of the expected $\omega^{-5/3}$ scaling and more closely follows the DNS spectrum. While the FLDI spectrum corrected with a finite density disturbance field shows a flatter adherence to the expected $\omega^{-5/3}$ slope, the DNS spectrum appears to tangentially approach the expected scaling. Continuing into the dissipation range ($95 \le \omega\delta/U_\infty \le 144$), the disparity between the two FLDI spectra increases, as well as the difference between the FLDI spectrum corrected assuming a finite disturbance field and the DNS spectrum. All spectra diverge considerably from the expected ω^{-5} scaling in this region. Although the FLDI spectrum accounting for a limited density disturbance field showed good adherence to the respective scalings of the energy-containing and inertial ranges, it maintained a gentler decay in the dissipation range. Similarly, a distinct change in slope is not observed with the DNS spectrum, and the spectra appear to tangentially approach the expected ω^{-5} scaling.

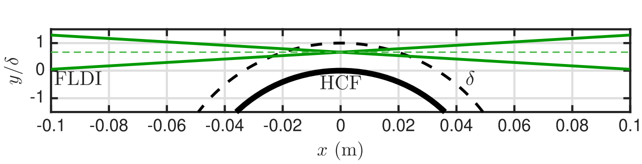

Fig. 7 Propagation of FLDI beams through the boundary layer generated over the hollow-cylinder section of the hollow-cylinder flare.

B. Correlation Comparison

The space-time correlation of the density field is defined as

$$C_{\rho\rho}(\Delta x, \Delta t) = \frac{\overline{\rho'(x,y,z,t)\rho'(x+\Delta x,y,z,t+\Delta t)}}{\left(\overline{\rho'^2(x,y,z,t)}\right)^{1/2}\left(\overline{\rho'^2(x+\Delta x,y,z,t+\Delta t)}\right)^{1/2}} \tag{3}$$

where Δx is the spatial separation in the streamwise direction and Δt is the time delay.

1. Autocorrelation

The autocorrelation of density fluctuations is given by setting Δx equal to zero in Eq. (3). Figure 8 presents the autocorrelation function (ACF) of density fluctuations measured experimentally by each FLDI detector. Each ACF was computed over a broadband frequency range extending from the onset of the energy-containing region to the end of the dissipation range. To obtain the ACFs, the phase change measured in the temporal domain by each FLDI detector was transformed into the spatial wavenumber domain

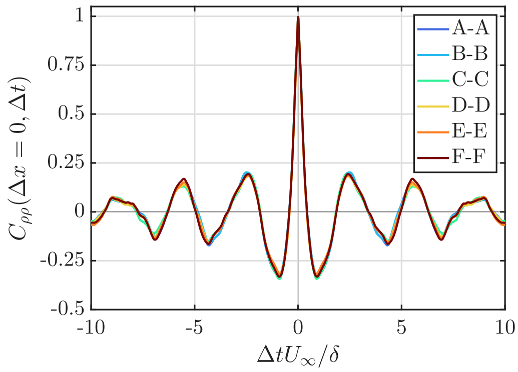

Fig. 8 Autocorrelation of density fluctuations for all FLDI detectors.

following the procedure defined by Hameed and Parziale [72], using the $\sin(\kappa x), -L \leq z \leq L$ transfer function. The resulting spectra were filtered to within the specified frequency bounds and then transformed back to the temporal domain, where the autocorrelation was calculated using MATLAB's `xcorr` function. Excellent agreement was observed between the ACFs of each FLDI detector, with matching temporal decay rates from the perfectly correlated value at $\Delta t_{\text{norm}} = \Delta t U_\infty/\delta = 0$. The signal became negatively correlated at $\Delta t_{\text{norm}} \approx 0.42$, with the anti-autocorrelation reaching a minimum of $C_{\rho\rho} \approx -0.33$ at approximately one normalized time delay. The oscillatory nature of each ACF continued with increasing normalized time delay; however, the local maxima and minima of the autocorrelation coefficients were observed to have significantly decreased.

Figure 9 shows a comparison between the experimentally and numerically calculated ACF of density fluctuations in the energy-containing range, inertial subrange, and dissipation range as a function of time delay. The process to calculate the ACF for FLDI data followed the steps previously described, with the frequency bandwidth limited to the specific ranges of the respective power-law scaling regions. The autocorrelation of density fluctuations extracted from the DNS flowfield was computed similarly without the need to apply transfer functions for spectral correction. There was generally good agreement between the autocorrelation computed from the experimental and numerical datasets, with an increase in the temporal decay rate observed for higher frequency density fluctuations. A significant degree of anti-autocorrelation was observed in each scaling region. For the lower frequency fluctuations present in the energy-containing range, the signal was approximately 25–35% negatively autocorrelated. In the inertial subrange, the signal's negative autocorrelation increased to 45–50%. In the dissipation range, the oscillatory nature of the density field at these higher frequencies was most apparent, as the signal was equally positively and negatively autocorrelated.

The agreement between the experimental and computational autocorrelation functions of density fluctuations varied between scaling regions. In the energy-containing range, where the corrected FLDI density spectrum slightly deviated from the DNS spectrum, and consequently, the referenced ω^{-1} scaling, the ACF derived from DNS data exhibited a faster temporal decay rate and a reduced degree of negative autocorrelation. Furthermore, the DNS ACF was observed to have higher frequency oscillations, which were absent in the FLDI ACF. In the inertial subrange, the excellent agreement between the FLDI and DNS density spectra corresponded to good agreement between the experimentally and computationally determined ACFs, with matching temporal decay rates and local maximum and minimum autocorrelation values. The higher frequency oscillations observed in the energy-containing range remained in this region; however, they appeared to have only a modest effect on the overall shape of the DNS ACF at longer normalized time delays. In the dissipation range, where the most significant differences were observed between the two spectra, the ACF comparison showed a similar degree of disagreement. While the temporal decay rate and period of oscillation showed good agreement, the DNS ACF was observed to have a slightly higher oscillatory magnitude until approximately $\Delta t_{\text{norm}} = \Delta t U_\infty/\delta \approx 0.5$. For a short duration after this normalized time delay, the DNS and FLDI autocorrelation functions matched until $\Delta t_{\text{norm}} \approx 0.75$, at which point, a moderate increase in autocorrelation was observed in the DNS ACF.

2. *Cross-Correlation*

The space-time correlation computed for successive FLDI beams spatially separated by multiples of the interbeam spacing (2.4 mm) is shown in Fig. 10. The procedure used to compute the space-time correlation was similar to that described in Sec. IV.B.1, with the same transfer function used to correct the FLDI spectra. For the results shown in Fig. 10, the correlation was bandpass filtered from the minimum frequency of the energy-containing range to the maximum frequency of the dissipation range ($2 \leq \omega\delta/U_\infty \leq 144$). The autocorrelation of FLDI probe A (labeled A-A in Fig. 10) was provided as a reference. The density fluctuations became less correlated as the spatial separation between the FLDI probes was increased; within one normalized time delay and spanning a distance of approximately 1.2δ, the density fluctuations decorrelated from unity to $C_{\rho\rho} \approx 0.8$. A monotonic, nearly linear decay was observed with a slight broadening of the correlation peak. While the peak cross-correlation values decreased, the negative cross-correlation between increasingly spaced probes remained consistent.

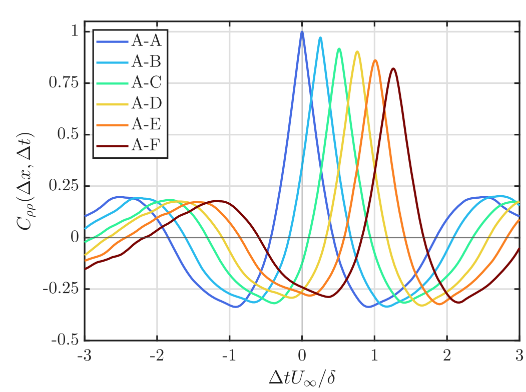

Fig. 10 Cross-correlation of density fluctuations between spatially separated FLDI probes, $C_{\rho\rho}(\Delta x, \Delta t)$, as a function of time delay, Δt.

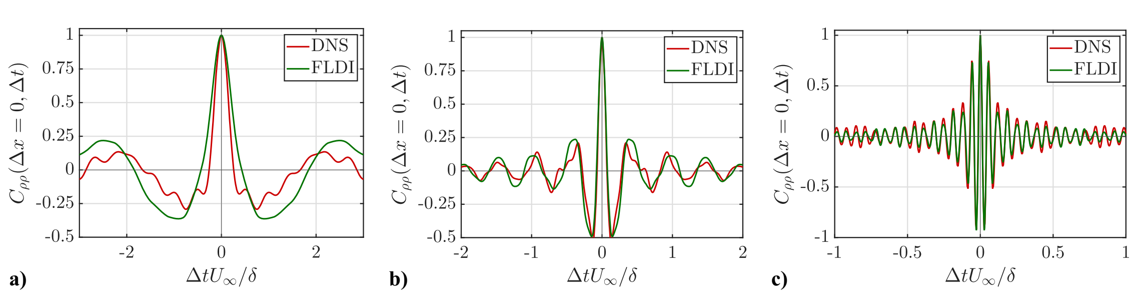

Fig. 9 Autocorrelation of density fluctuations, $C_{\rho\rho}(\Delta x = 0, \Delta t)$, computed from experimental and numerical data in the a) energy-containing, b) inertial, and c) dissipation range.

The individual peaks of the FLDI and DNS cross-correlation coefficients as a function of streamwise separation normalized by the respective boundary-layer thickness, $\Delta x/\delta$, are shown in Fig. 11. Similar to the autocorrelation presented above, the cross-correlation comparison is also presented within the estimated energy-containing, inertial, and dissipation ranges. The FLDI cross-correlation coefficients are presented as six discrete points corresponding to the distinct measurement locations, and the DNS cross-correlation coefficients are shown as a continuous function.

In the energy-containing range (Fig. 11a), the DNS and FLDI cross-correlations show very good agreement across the plotted normalized spatial separations. At these low frequencies, density fluctuations remain strongly correlated over substantial distances, with the peak cross-correlation coefficient decreasing from unity to 0.85 over a streamwise distance equivalent to approximately one boundary-layer thickness. In the intermediate frequencies of the inertial subrange (Fig. 11b), excellent agreement between FLDI and DNS is again observed across all measured normalized streamwise separations. Here, the density fluctuations decorrelate moderately, with the correlation coefficient decreasing from unity to roughly 0.5 over approximately one boundary-layer thickness. Finally, Fig. 11c presents the peaks of the cross-correlation coefficients in the high-frequency dissipation range. At these frequencies, density fluctuations decorrelate rapidly, and notable discrepancies emerge between the FLDI and DNS datasets. FLDI measurements exhibit a faster spatial decay, with fluctuations becoming 50% decorrelated within about 0.2δ and reaching a minimum of $C_{\rho\rho} \approx 0.04$ at $\Delta x/\delta \approx 0.7$. In contrast, the DNS cross-correlation decays more gradually, with a 50% decorrelation occurring near 0.35δ and continuing to decrease with increasing separation. While the divergence between FLDI and DNS initially grows due to these differing decay rates, it stabilizes as the correlation coefficients asymptotically approach their respective minima. The good agreement between the FLDI and DNS datasets in the energy-containing and inertial ranges and poor agreement in the dissipation range is consistent with the spectral results presented in Fig. 6.

C. Coherence Comparison

The magnitude-squared coherence of density fluctuations computed from the FLDI and DNS datasets is presented in the outer length scale in Fig. 12. The coherence obtained using the FLDI diagnostic was computed by first converting the measured phase change to density using the $\sin(\kappa x), -L \leq z \leq L$ transfer function and then applying MATLAB's `mscohere` function. For the DNS density data, the coherence function was defined by Eq. (4), with Δx prescribed to match the normalized spatial separation values $(\Delta x/\delta)$ of the individual FLDI beam pairs, compensating for the difference between the experimental and computational boundary-layer thickness and maintaining $y/\delta = 0.66$.

$$\Gamma^2_{ab}(\Delta x/\delta, \Delta y, \omega) = \frac{|\Phi_{P_a P_b}(\Delta x/\delta, \Delta y, \omega)|^2}{|\Phi_{P_a P_a}(\omega)||\Phi_{P_b P_b}(\omega)|} \tag{4}$$

In general, good agreement was observed between the coherence of density fluctuations computed using the FLDI data and DNS data at shorter streamwise separation distances. Considering the coherence spectra at the streamwise separation of $\Delta x/\delta \approx 0.22$, the

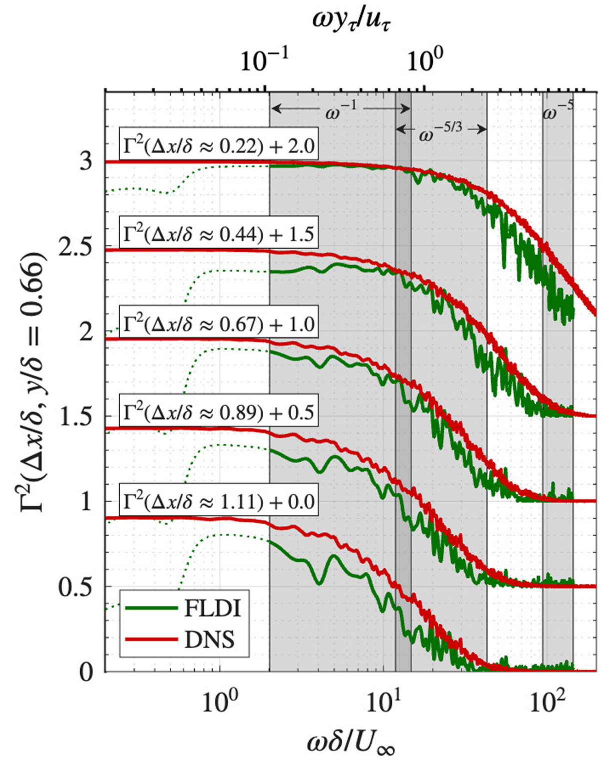

Fig. 12 Coherence of density fluctuations between streamwise probe locations calculated from FLDI and DNS data. Dotted sections of FLDI spectra represent frequencies beyond the instrument's range.

magnitude-squared coherence was observed to be slightly below unity throughout the energy-containing range. A gradual roll-off, spanning approximately a decade of the normalized frequency, was observed in both the FLDI and DNS magnitude-squared coherence, beginning near the onset of the inertial subrange at $\omega\delta/U_\infty \approx 15$ and continuing until the coherence diminished to its minimum value in the dissipation range. At this relatively short streamwise probe separation, for both the FLDI and DNS datasets, the coherence maintained a nonzero value across the measured frequency range, without an asymptotic approach to zero. Additionally, the magnitude-squared coherence computed from FLDI data was observed to roll off at a slightly lower frequency than the coherence computed from DNS data, resulting in DNS coherence values deviating marginally in the roll-off region.

Increasing the streamwise separation to $\Delta x/\delta \approx 0.44$ resulted in a DNS coherence spectrum with an initial value of $\Gamma^2 \approx 0.97$. The coherence computed from the experimental FLDI dataset was appreciably lower within the energy-containing range. However, within the inertial subrange, both FLDI and DNS coherence spectra experienced similar roll-off characteristics, with consistent roll-off onset, and the DNS spectrum maintained slightly higher coherence values throughout the roll-off region. At this streamwise separation, the calculated coherence from both datasets changed concavity and showed an asymptotic approach to zero after the roll-off period. As the streamwise separation was further increased, the initial

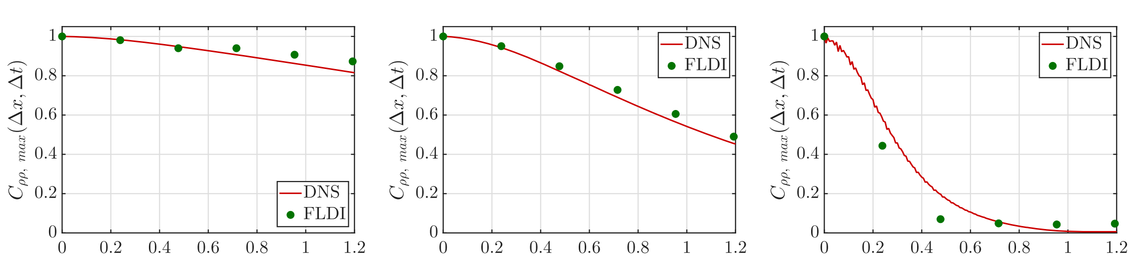

Fig. 11 Cross-correlation of density fluctuations, $C_{\rho\rho}(\Delta x, \Delta t)$, computed from experimental and numerical data in the a) energy-containing, b) inertial, and c) dissipation range.

coherence values computed from computational data decreased slightly. With increasing separation, the roll-off region shifted to progressively lower frequencies, and a greater discrepancy between the computationally and experimentally computed coherence values was observed. The DNS coherence spectra consistently showed higher values throughout the energy-containing range and inertial subrange at these larger spatial separations. The roll-off in coherence comprised the entirety of the inertial subrange. After the roll-off, both coherence spectra for each of these larger streamwise probe separations exhibited an extended frequency range of nearly zero correlation, with the dissipation range nearly fully decorrelated. At the larger probe separations examined ($\Delta x/\delta \geq 0.89$), the initial coherence values computed using DNS data decreased to $\Gamma^2 \approx 0.9$, suggesting significant levels of correlation remained among low-frequency disturbances. At the start of the energy-containing range, the DNS coherence value was largely unchanged, while the coherence computed using FLDI data was significantly lower, at $\Gamma^2 \approx 0.76$. The roll-off in the coherence calculated from both datasets was observed to begin immediately at the beginning of the energy-containing range, with the computed coherence decreasing to $\Gamma^2_{\mathrm{DNS}} \approx 0.5$ and $\Gamma^2_{\mathrm{FLDI}} \approx 0.38$ by the end. For both datasets, the roll-off continued in the inertial subrange, within which the coherence decreased to approximately zero. At this streamwise separation of approximately one boundary-layer thickness, the disturbances in the dissipation range were fully decorrelated.

V. Conclusions

This work compares experimental measurements of density fluctuations over a hollow-cylinder flare to DNS simulations performed under similar conditions. The experimental observations were made using a multipoint FLDI diagnostic (6 FLDI beam pairs), separated in a single row within the boundary layer at $y/\delta = 0.66$. The DNS simulation was performed using the provided experimental nozzle exit conditions and model geometry. A comparison between the experimental and computational power spectral density, auto- and cross-correlation, and coherence was presented.

There was generally good agreement between the power spectral density computed using density fluctuation data obtained from the experiment and from the DNS simulation. The comparison was further analyzed within the energy-containing range (ω^{-1}), the inertial subrange ($\omega^{-5/3}$), and the dissipation range (ω^{-5}). Good agreement was observed in the energy-containing range, with the largest discrepancy at the lower normalized frequencies. Excellent agreement between the experimental and DNS spectra was obtained in the inertial subrange. The greatest discrepancy was observed in the dissipation range, where the DNS spectra experienced a higher rate of decrease than the experimental spectra. We do not believe the discrepancy at high frequency is due to FLDI instrument bandwidth. The beam intraspacing that was prescribed as part of the flow diagnostic design was approximately 40 µm, resulting in a Nyquist frequency based on beam separation of approximately 13 MHz. This is higher than the reported frequency content in the boundary layer, where the SNR is above the noise floor to ≈4 MHz (see Fig. 5).

Regarding the density autocorrelation functions computed from experimental and computational data, we observed discrepancies in the correlation comparison similar to those observed in the spectral comparison. Namely, the autocorrelation functions in the energy-containing and dissipative ranges diverged between the two datasets. The divergence in the energy-containing range was attributed to the low-frequency density fluctuations, which were not properly resolved by the small FLDI beam intraspacing. In the dissipation range, we observed a wider discrepancy; the autocorrelation function generated from experimental data showed a slightly faster decay rate, decaying below $C_{\rho\rho} = 0.25$ within $\Delta t U_\infty/\delta = 0.1$. Interestingly, both autocorrelation functions exhibited a beat frequency. The best agreement between the two autocorrelation functions was observed in the inertial subrange, where the amplitude and period of the oscillations showed excellent agreement.

Comparing the cross-correlation of density fluctuations obtained experimentally and computationally, we observed generally good agreement between the datasets. The lower-frequency fluctuations in the energy-containing range remained largely correlated. As the disturbance frequency was increased, the decrease in the cross-correlation coefficient was more pronounced, with the cross-correlation coefficient decreasing to negligible values within half a boundary-layer thickness in the streamwise direction for the dissipation range.

Regarding the coherence of density fluctuations between streamwise probe locations, we observed good agreement overall, with the best agreement occurring at the smallest streamwise separations. At the shortest streamwise separation ($\Delta x/\delta \approx 0.22$), the fluctuations remained correlated until the inertial subrange. As the separation was increased, the coherence decreased dramatically, and at a spatial separation equal to approximately one boundary-layer thickness, the fluctuations in the energy-containing range exhibited diminished coherence values, and those in the inertial subrange were almost completely incoherent.

Appendix: Grid Refinement Study on DNS of the Hollow Cylinder/Flare Configuration

This appendix provides a detailed assessment of grid refinement effects to verify that the spatial and temporal resolutions used in the DNS are adequate for calculating spectral, correlation, and coherence statistics of density (ρ) fluctuations in the hypersonic hollow-cylinder/flare (HCF) configuration. The objective is to show that the grid resolution has only a minimal effect on the quantities analyzed in the main text and to justify the grid selected for the primary simulation.

Table 5 presents the DNS resolution metrics for the different grids examined in this work. Alongside the baseline DNS, two additional DNS cases with grids that are respectively coarser and finer than the baseline were conducted to assess sensitivity to grid resolution. These three DNS configurations (coarse, baseline, and fine), which encompass only the HC section of the HCF geometry, are also compared to the Box 2 DNS from Roy et al. [71]. In the latter case, the streamwise domain starts slightly upstream of the sampling plane above the HC and continues through the flare region of the HCF, and the simulation was calculated using twice the number of spanwise grid points. Figure 13a depicts the streamwise extents of all the simulations. All simulations employ a structured, body-fitted mesh with grid clustering near the wall to capture viscous near-wall dynamics, and the wall-normal grid distribution for each case is illustrated in Fig. 13b. An azimuthal domain of $\phi = 60°$ is used consistently in all cases.

Figure 14 compares the PSD of density fluctuations at the wall of $y/\delta = 0$ and in the outer layer of $y/\delta \approx 0.6$. At both positions, the PSD from all grid configurations collapses satisfactorily across the energetic range of the spectrum and then transitions smoothly into a high-frequency decay with a slope characteristic of dissipation-range dynamics in compressible wall-bounded turbulence. At the highest-frequency end ($\omega y_\tau/u_\tau \gtrsim 5$), which lies well within the

Table 5 Grid-resolution metrics for the convergence study of HC simulations computed at the reference plane shown in Fig. 13a (the azimuthal spanwise domain size is $\phi = 60°$)

Case	x_{beg}, m	x_{end}, m	$N_x \times N_\phi \times N_r$	Δx^+	$(r\Delta\phi)^+_w$	$(r\Delta\phi)^+_\delta$	Δy^+_w	$\Delta y^+_{0.6\delta}$	Δy^+_δ
Coarse	0.305	0.898	$3300 \times 500 \times 500$	6.74	3.97	4.86	0.71	5.47	5.55
Baseline	0.305	0.898	$4700 \times 750 \times 750$	4.73	2.65	3.24	0.47	3.64	3.71
Fine	0.847	0.898	$744 \times 750 \times 1125$	3.03	2.65	3.24	0.31	2.14	2.48
Roy et al. (2025)	0.847	1.04	$3000 \times 1500 \times 750$	4.73	1.33	1.62	0.13	2.49	3.86

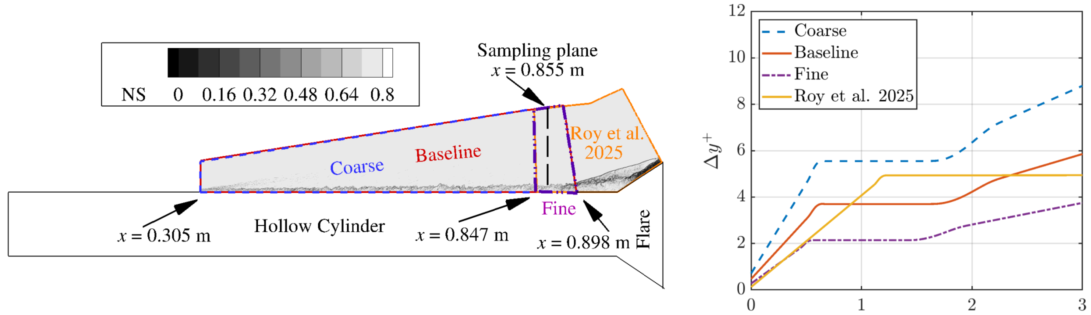

Fig. 13 Grid study overview: a) domain extents and b) wall-normal grid distribution comparison.

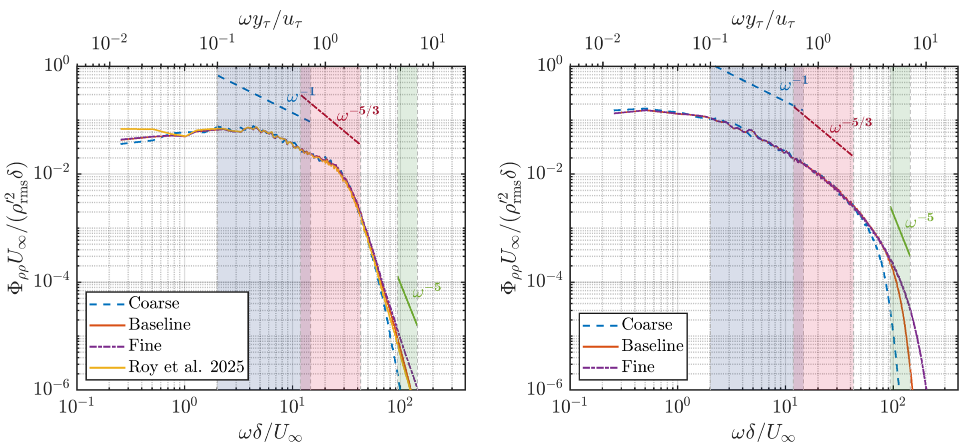

a) $\Phi_{\rho\rho}(\omega)$ at $y/\delta = 0$

b) $\Phi_{\rho\rho}(\omega)$ at $y/\delta \approx 0.6$

Fig. 14 Power spectral density of density fluctuations for different grid resolutions. The shaded regions represent the characteristic turbulence scales.

dissipation range and accounts for less than 0.5% of the total fluctuation energy, differences in the spectral roll-off become apparent among the grids with varying streamwise and wall-normal resolutions. In contrast, the comparison between the baseline grid and the configuration of Roy et al. [71] at the wall indicates that increasing the spanwise resolution does not alter the roll-off slope.

Figures 15 and 16 present comparisons of the temporal autocorrelation and maximum cross-correlation functions over various

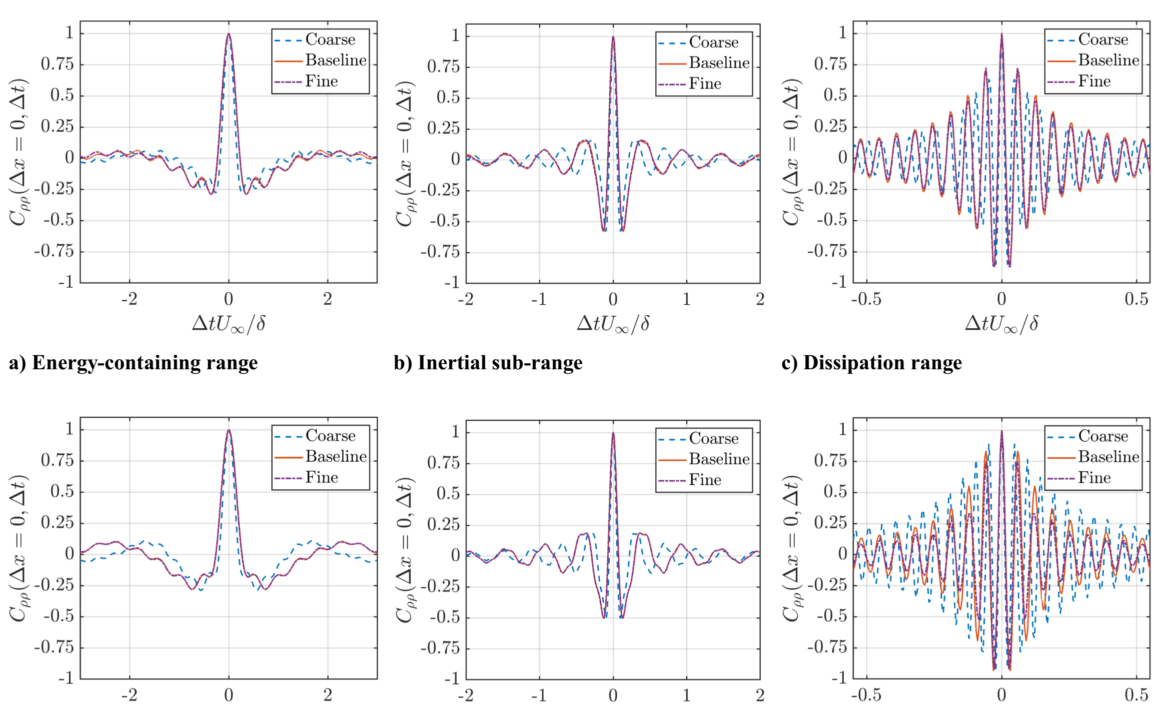

a) Energy-containing range **b) Inertial sub-range** **c) Dissipation range**

d) Energy-containing range **e) Inertial sub-range** **f) Dissipation range**

Fig. 15 Autocorrelation functions of the density fluctuations ρ' across different spectral ranges. Top row: $y/\delta = 0$. Bottom row: $y/\delta \approx 0.6$.

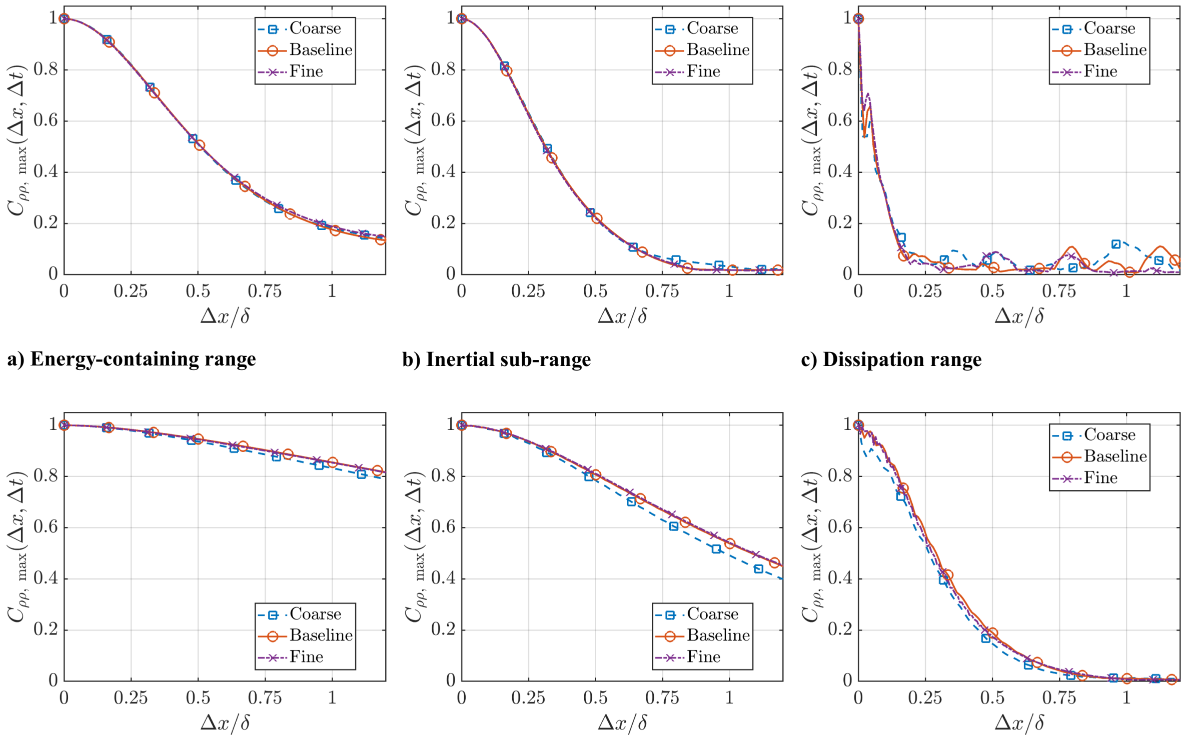

a) Energy-containing range b) Inertial sub-range c) Dissipation range

d) Energy-containing range e) Inertial sub-range f) Dissipation range

Fig. 16 Maximum cross-correlation of density fluctuations ρ' across different spectral ranges. Top row: $y/\delta = 0$. Bottom row: $y/\delta \approx 0.6$.

spectral ranges for the different grid configurations, respectively. The selection of each spectral range (energy-containing, inertial subrange, dissipation) is consistent with those in the FLDI/DNS comparisons shown in Figs. 9 and 11. At both $y/\delta = 0$ and 0.6, the baseline and fine-grid cases yield nearly indistinguishable correlation functions across all spectral ranges, whereas the coarse-grid case exhibits a slight deviation from these two.

Figure 17 shows the streamwise coherence function Γ^2 of the density fluctuations at $y/\delta = 0$ (left) and $y/\delta \approx 0.6$ (right). The coherence obtained from the baseline and fine-grid simulations agrees closely across almost the entire frequency range, further demonstrating that the baseline grid resolution is sufficient to capture both the spectral characteristics and spatial structure of the density fluctuations.

In summary, the DNS grid sensitivity analysis confirms that the baseline grid is appropriate for resolving the dynamically significant scales in the present study and spans the frequency range pertinent to the current FLDI/DNS comparisons.

Acknowledgments

The authors would like to thank Dr. Eric Marineau for his support. Support for Ahsan Hameed, Ben Segall, Jaden Kokinakos, and

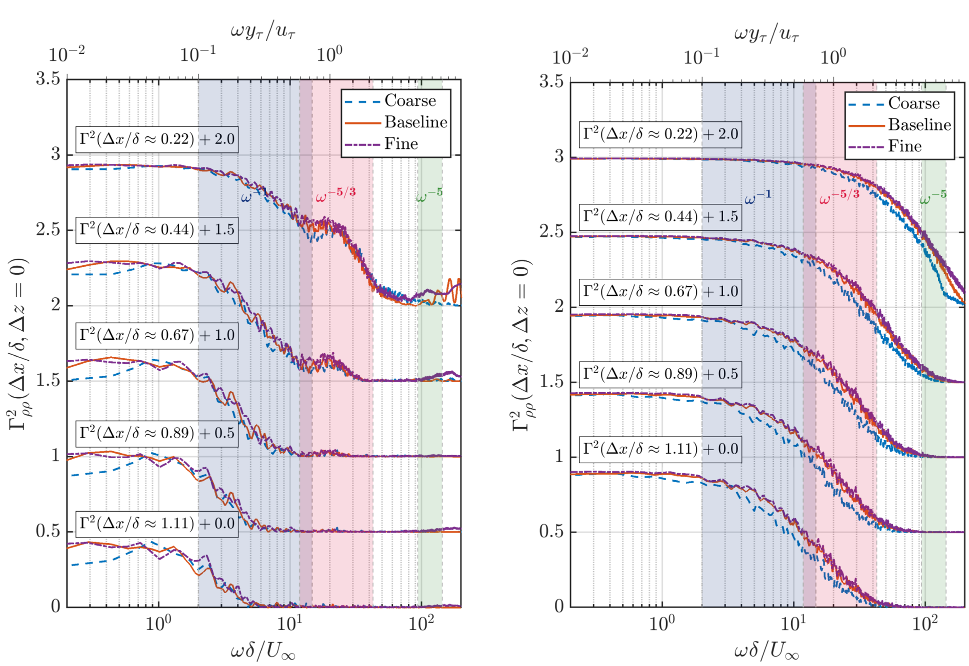

a) Wall coherence ($y/\delta = 0$) b) Outer-layer coherence ($y/\delta \approx 0.6$)

Fig. 17 Streamwise coherence Γ^2 of density fluctuations at the wall and in the outer layer.

Nick Parziale was provided from Office of Naval Research (ONR) grant N00014-23-1-2474. Additional support was provided from United States Army Small Business Technology Transfer–Phase II grant W911NF25CA009. Support for Dhiman Roy and Lian Duan was provided from ONR grant N00014-23-1-2304.

References

[1] Schneider, S. P., "Flight Data for Boundary-Layer Transition at Hypersonic and Supersonic Speed," *Journal of Spacecraft and Rockets*, Vol. 36, No. 1, 1999, pp. 8–20.
https://doi.org/10.2514/2.3428

[2] MacLean, M., Wadhams, T., Holden, M., and Johnson, H., "Ground Test Studies of the HIFiRE-1 Transition Experiment Part 2: Computational Analysis," *Journal of Spacecraft and Rockets*, Vol. 45, No. 6, 2008, pp. 1149–1164.
https://doi.org/10.2514/1.37693

[3] Jewell, J. S., Parziale, N. J., Leyva, I. A., Shepherd, J. E., and Hornung, H. G., "Turbulent Spot Observations Within a Hypervelocity Boundary Layer on a 5-Degree Half-Angle Cone," *Proceedings of 42nd AIAA Fluid Dynamics Conference and Exhibit*, AIAA Paper 2012-3062, 2012.
https://doi.org/10.2514/6.2012-3062

[4] Willmarth, W. W., and Yang, C. S., "Wall-Pressure Fluctuations Beneath Turbulent Boundary Layers on a Flat Plate and a Cylinder," *Journal of Fluid Mechanics*, Vol. 41, No. 1, 1970, pp. 47–80.
https://doi.org/10.1017/S0022112070000526

[5] Bull, M. K., "Wall-Pressure Fluctuations Beneath Turbulent Boundary Layers: Some Reflections on Forty Years of Research," *Journal of Sound and Vibration*, Vol. 190, No. 3, 1996, pp. 299–315.
https://doi.org/10.1006/jsvi.1996.0066

[6] Ceruzzi, A. P., and Cadou, C. P., "Simultaneous Velocity and Density Gradient Measurements Using Two-Point Focused Laser Differential Interferometry," *AIAA Scitech 2019*, AIAA Paper 2019-2295, 2019.
https://doi.org/10.2514/6.2019-2295

[7] Smeets, G., and George, A., "Gas Dynamic Investigations in a Shock Tube Using a Highly Sensitive Interferometer," Translation of ISL Internal Report 14/71, Original 1971, Translation 1996.

[8] Smeets, G., "Laser Interferometer for High Sensitivity Measurements on Transient Phase Objects," *IEEE Transactions on Aerospace and Electronic Systems*, Vol. 8, No. 2, 1972, pp. 186–190.
https://doi.org/10.1109/TAES.1972.309488

[9] Smeets, G., and George, A., "Anwendungen des Laser-Differentialinterferometers in der Gasdynamik," Institute Franco-Allemand de Recherches de Saint-Louis (ISL), ISL-28/73, Also translated by Goetz, A.: ADA-307459, 1973.

[10] Smeets, G., "Laser-Interferometer mit grossen, fokussierten Lichtbündeln für lokale Messungen," ISL-11/73, 1973.

[11] Smeets, G., "Verwendung eines Laser-Differentialinterferometers zur Bestimmung lokaler Schwankungsgrössen sowie des mittleren Dichteprofils in cinem turbulenten Freistrahl," ISL-20/74, 1974.

[12] Smeets, G., "Flow Diagnostics by Laser Interferometry," *IEEE Transactions on Aerospace and Electronic Systems*, Vol. 13, No. 2, 1977, pp. 82–90.
https://doi.org/10.1109/TAES.1977.308441

[13] Smeets, G., and George, A., "Laser Differential Interferometer Applications in Gas Dynamics," Translation of ISL Internal Report 28/73, Original 1975, Translation 1996.

[14] Parziale, N. J., Shepherd, J. E., and Hornung, H. G., "Reflected Shock Tunnel Noise Measurement by Focused Differential Interferometry," *Proceedings of 42nd AIAA Fluid Dynamics Conference and Exhibit*, AIAA Paper 2012-3261, 2012.
https://doi.org/10.2514/6.2012-3261

[15] Parziale, N. J., Jewell, J. S., Shepherd, J. E., and Hornung, H. G., "Optical Detection of Transitional Phenomena on Slender Bodies in Hypervelocity Flow," *Proceedings of RTO Specialists Meeting AVT-200/RSM-030 on Hypersonic Laminar-Turbulent Transition*, NATO, San Diego, CA, 2012.

[16] Parziale, N. J., Shepherd, J. E., and Hornung, H. G., "Differential Interferometric Measurement of Instability at Two Points in a Hypervelocity Boundary Layer," *Proceedings of 51st AIAA Aerospace Sciences Meeting Including the New Horizons Forum and Aerospace Exposition*, AIAA Paper 2013-0521, 2013.
https://doi.org/10.2514/6.2013-521

[17] Parziale, N. J., Shepherd, J. E., and Hornung, H. G., "Differential Interferometric Measurement of Instability in a Hypervelocity Boundary Layer," *AIAA Journal*, Vol. 51, No. 3, 2013, pp. 750–753.
https://doi.org/10.2514/1.J052013

[18] Parziale, N. J., "Slender-Body Hypervelocity Boundary-Layer Instability," Ph.D. Thesis, California Inst. of Technology, Pasadena, CA, 2013.

[19] Parziale, N. J., Shepherd, J. E., and Hornung, H. G., "Free-Stream Density Perturbations in a Reflected-Shock Tunnel," *Experiments in Fluids*, Vol. 55, No. 2, 2014, p. 1665.
https://doi.org/10.1007/s00348-014-1665-0

[20] Parziale, N. J., Shepherd, J. E., and Hornung, H. G., "Observations of Hypervelocity Boundary-Layer Instability," *Journal of Fluid Mechanics*, Vol. 781, Oct. 2015, pp. 87–112.
https://doi.org/10.1017/jfm.2015.489

[21] Jewell, J. S., Parziale, N. J., Lam, K.-L., Hagen, B. J., and Kimmel, R. L., "Disturbance and Phase Speed Measurements for Shock Tubes and Hypersonic Boundary-Layer Instability," *32nd AIAA Aerodynamic Measurement Technology and Ground Testing Conference*, AIAA Paper 2016-3112, 2016.
https://doi.org/10.2514/6.2016-3112

[22] Jewell, J. S., Hameed, A., Parziale, N. J., and Gogineni, S. P., "Disturbance Speed Measurements in a Circular Jet via Double Focused Laser Differential Interferometry," *AIAA Scitech 2019*, AIAA Paper 2019-2293, 2019.
https://doi.org/10.2514/6.2019-2293

[23] Ceruzzi, A. P., Callis, B., Weber, D., and Cadou, C. P., "Application of Focused Laser Differential Interferometry (FLDI) in a Supersonic Boundary Layer," *AIAA Scitech 2020*, AIAA Paper 2020-1973, 2020.
https://doi.org/10.2514/6.2020-1973

[24] Weisberger, J. M., Bathel, B. F., Herring, G. C., King, R. A., Chou, A., and Jones, S. B., "Two-Point Focused Laser Differential Interferometry Second-Mode Measurements at Mach 6," *AIAA Aviation Forum*, AIAA Paper 2019-2903, 2019.
https://doi.org/10.2514/6.2019-2903

[25] Bathel, B. F., Weisberger, J. M., Herring, G. C., King, R. A., Jones, S. B., Kennedy, R. E., and Laurence, S. J., "Two-Point, Parallel-Beam Focused Laser Differential Interferometry with a Nomarski Prism," *Applied Optics*, Vol. 59, No. 2, 2020, pp. 244–252.
https://doi.org/10.1364/AO.59.000244

[26] Price, T. J., Gragston, M., Schmisseur, J. D., and Kreth, P. A., "Measurement of Supersonic Jet Screech with Focused Laser Differential Interferometry," *Applied Optics*, Vol. 59, No. 28, 2020, pp. 8902–8908.
https://doi.org/10.1364/AO.402011

[27] Hameed, A., Parziale, N. J., Paquin, L., Butler, C., and Laurence, S. J., "Spectral Analysis of a Hypersonic Boundary Layer on a Right, Circular Cone," *AIAA Scitech 2020*, AIAA Paper 2020-0362, 2020.
https://doi.org/10.2514/6.2020-0362

[28] Harris, A. J., Kreth, P. A., Combs, C. S., and Schmisseur, J. D., "Laser Differential Interferometry and Schlieren as an Approach to Characterizing Freestream Disturbance Levels," *2018 AIAA Aerospace Sciences Meeting*, AIAA Paper 2018-1100, 2018.
https://doi.org/10.2514/6.2018-1100

[29] Lawson, J. M., and Austin, J. M., "Expansion Tube Freestream Disturbance Measurements Using a Focused Laser Differential Interferometer," *AIAA Scitech 2020*, AIAA Paper 2020-1064, 2020.
https://doi.org/10.2514/6.2020-1064

[30] Birch, B., Buttsworth, D., and Zander, F., "Measurements of Freestream Density Fluctuations in a Hypersonic Wind Tunnel," *Experiments in Fluids*, Vol. 61, No. 158, 2020, pp. 1–13.
https://doi.org/10.1007/s00348-020-02992-w

[31] Hedlund, B., Houpt, A., Gordeyev, S., and Leonov, S., "Measurement of Flow Perturbation Spectra in Mach 4.5 Corner Separation Zone," *AIAA Journal*, Vol. 56, No. 7, 2018, pp. 2699–2711.
https://doi.org/10.2514/1.J056576

[32] Houpt, A. W., and Leonov, S. B., "Focused Laser Differential Interferometer for Supersonic Boundary Layer Measurements on Flat Plate Geometries," *2018 Plasmadynamics and Lasers Conference*, AIAA Paper 2018-3434, 2018.
https://doi.org/10.2514/6.2018-3434

[33] Houpt, A. W., and Leonov, S. B., "Focused and Cylindrical-Focused Laser Differential Interferometer Characterization of SBR-50 at Mach 2," *AIAA Aviation 2019*, AIAA Paper 2019-3383, 2019.
https://doi.org/10.2514/6.2019-3383

[34] Benitez, E. K., Jewell, J. S., and Schneider, S. P., "Focused Laser Differential Interferometry for Hypersonic Flow Instability Measurements with Contoured Tunnel Windows," *AIAA Scitech 2020*, AIAA Paper 2020-1282, 2020.
https://doi.org/10.2514/6.2020-1282

[35] Benitez, E. K., Esquieu, S., Jewell, J. S., and Schneider, S. P., "Instability Measurements on an Axisymmetric Separation Bubble at Mach 6," *AIAA Aviation 2020*, AIAA Paper 2020-3072, 2020.
https://doi.org/10.2514/6.2020-3072

[36] Ramprakash, A., McIntyre, T. J., Wheatley, V., and Mee, D. J., "Performance Analysis of FLDI Technique Using Turbulent Jets," *Proceedings of the IX Australian Conference on Laser Diagnostics*, The Australian and New Zealand Optical Soc., 2019.
[37] Lawson, J. M., Neet, M. C., Grossman, I. J., and Austin, J. M., "Characterization of a Focused Laser Differential Interferometer," *AIAA Scitech 2019*, AIAA Paper 2019-2296, 2019. https://doi.org/10.2514/6.2019-2296
[38] Lawson, J. M., Neet, M. C., Grossman, I. J., and Austin, J. M., "Static and Dynamic Characterization of a Focused Laser Differential Interferometer," *Experiments in Fluids*, Vol. 61, No. 187, 2020, pp. 1–11. https://doi.org/10.1007/s00348-020-03013-6
[39] Fulghum, M. R., "Turbulence Measurements in High-Speed Wind Tunnels Using Focusing Laser Differential Interferometry," Ph.D. Thesis, Pennsylvania State Univ., Pennsylvania, PA, 2014.
[40] Settles, G. S., and Fulghum, M. R., "The Focusing Laser Differential Interferometer, an Instrument for Localized Turbulence Measurements in Refractive Flows," *Journal of Fluids Engineering*, Vol. 138, No. 10, 2016, Paper 101402. https://doi.org/10.1115/1.4033960
[41] Schmidt, B. E., and Shepherd, J. E., "Analysis of Focused Laser Differential Interferometry," *Applied Optics*, Vol. 54, No. 28, 2015, pp. 8459–8472. https://doi.org/10.1364/AO.54.008459
[42] Hameed, A., and Parziale, N. J., "Focused Laser Differential Interferometry Transfer Functions for Complex Density Disturbance Fields," *AIAA Aviation Forum 2021*, AIAA Paper 2021-2907, 2021. https://doi.org/10.2514/6.2021-2907
[43] Williams, O. J. H., Sahoo, D., Baumgartner, M. L., and Smits, A. J., "Experiments on the Structure and Scaling of Hypersonic Turbulent Boundary Layers," *Journal of Fluid Mechanics*, Vol. 834, Jan. 2018, pp. 237–270. https://doi.org/10.1017/jfm.2017.712
[44] Kistler, A. L., and Chen, W. S., "The Fluctuating Pressure Field in a Supersonic Turbulent Boundary Layer," *Journal of Fluid Mechanics*, Vol. 16, No. 1, 1963, pp. 41–64. https://doi.org/10.1017/S0022112063000574
[45] Beresh, S. J., Henfling, J. F., Spillers, R. W., and Pruett, B. O., "Fluctuating Wall Pressures Measured Beneath a Supersonic Turbulent Boundary Layer," *Physics of Fluids*, Vol. 23, No. 7, 2011, Paper 075110. https://doi.org/10.1063/1.3609271
[46] Fernholz, H. H., Dussauge, J. P., Finlay, P. J., Smits, A. J., and Reshotko, E., "A Survey of Measurements and Measuring Techniques in Rapidly Distorted Compressible Turbulent Boundary Layers," AGARD-315, 1989.
[47] Camillo, G. P., Wagner, A., Toki, T., and Scalo, C., "Combined Experimental and Numerical Investigation of a Hypersonic Turbulent Boundary Layer by Means of FLDI and Large-Eddy Simulations," *Aerospace*, Vol. 10, No. 6, 2023, p. 570. https://doi.org/10.3390/aerospace10060570
[48] Benitez, E. K., Aultman, M., Duan, L., Camillo, G. P., and Jewell, J. S., "Significance of the Smaller Scales for Hypersonic Turbulent Boundary Layers with Focused Laser Differential Interferometry," *Physics of Fluids*, Vol. 36, No. 11, 2024. https://doi.org/10.1063/5.0235247
[49] Simens, M. P., Jiménez, J., Hoyas, S., and Mizuno, Y., "A High-Resolution Code for Turbulent Boundary Layers," *Journal of Computational Physics*, Vol. 228, No. 11, 2009, pp. 4218–4231. https://doi.org/10.1016/j.jcp.2009.02.031
[50] Pirozzoli, S., and Bernardini, M., "Turbulence in Supersonic Boundary Layers at Moderate Reynolds Number," *Journal of Fluid Mechanics*, Vol. 688, Dec. 2011, pp. 120–168. https://doi.org/10.1017/jfm.2011.368
[51] Adler, M. C., Gonzalez, D. R., Stack, C. M., and Gaitonde, D. V., "Synthetic Generation of Equilibrium Boundary Layer Turbulence from Modeled Statistics," *Computers & Fluids*, Vol. 165, March 2018, pp. 127–143. https://doi.org/10.1016/j.compfluid.2018.01.003
[52] Wenzel, C., Selent, B., Kloker, M., and Rist, U., "DNS of Compressible Turbulent Boundary Layers and Assessment of Data/Scaling-Law Quality," *Journal of Fluid Mechanics*, Vol. 842, May 2018, pp. 428–468. https://doi.org/10.1017/jfm.2018.179
[53] Ceci, A., Palumbo, A., Larsson, J., and Pirozzoli, S., "Numerical Tripping of High-Speed Turbulent Boundary Layers," *Theoretical and Computational Fluid Dynamics*, Vol. 36, No. 6, 2022, pp. 865–886. https://doi.org/10.1007/s00162-022-00623-0
[54] Huang, J., Duan, L., and Choudhari, M. M., "Direct Numerical Simulation of Hypersonic Turbulent Boundary Layers: Effect of Spatial Evolution and Reynolds Number," *Journal of Fluid Mechanics*, Vol. 937, April 2022, Paper A3. https://doi.org/10.1017/jfm.2022.80
[55] Martin, M. P., "Direct Numerical Simulation of Hypersonic Turbulent Boundary Layers. Part 1. Initialization and Comparison with Experiments," *Journal of Fluid Mechanics*, Vol. 570, Jan. 2007, pp. 347–364. https://doi.org/10.1017/S0022112006003107
[56] Duan, L., Beekman, I., and Martin, M. P., "Direct Numerical Simulation of Hypersonic Turbulent Boundary Layers. Part 2. Effect of Wall Temperature," *Journal of Fluid Mechanics*, Vol. 655, July 2010, pp. 419–445. https://doi.org/10.1017/S0022112010000959
[57] Duan, L., Beekman, I., and Martin, M. P., "Direct Numerical Simulation of Hypersonic Turbulent Boundary Layers. Part 3. Effect of Mach Number," *Journal of Fluid Mechanics*, Vol. 672, April 2011, pp. 245–267. https://doi.org/10.1017/S0022112010005902
[58] Duan, L., and Martin, M. P., "Direct Numerical Simulation of Hypersonic Turbulent Boundary Layers. Part 4. Effect of High Enthalpy," *Journal of Fluid Mechanics*, Vol. 684, Oct. 2011, pp. 25–59. https://doi.org/10.1017/jfm.2011.252
[59] Duan, L., Choudhari, M. M., and Zhang, C., "Pressure Fluctuations Induced by a Hypersonic Turbulent Boundary Layer," *Journal of Fluid Mechanics*, Vol. 804, Oct. 2016, pp. 578–607. https://doi.org/10.1017/jfm.2016.548
[60] Huang, J., Nicholson, G. L., Duan, L., Choudhari, M. M., and Bowersox, R. D. W., "Simulation and Modeling of Cold-Wall Hypersonic Turbulent Boundary Layers on Flat Plate," *AIAA Scitech 2020*, AIAA Paper 2020-0571, 2020. https://doi.org/10.2514/6.2020-0571
[61] Zhang, C., Duan, L., and Choudhari, M. M., "Direct Numerical Simulation Database for Supersonic and Hypersonic Turbulent Boundary Layers," *AIAA Journal*, Vol. 56, No. 11, 2018, pp. 4297–4311. https://doi.org/10.2514/1.J057296
[62] Gragston, M., Price, T. J., Davenport, K., Zhang, Z., and Schmisseur, J. D., "Linear Array Focused-Laser Differential Interferometry for Single-Shot Multi-Point Flow Disturbance Measurements," *Optics Letters*, Vol. 46, No. 1, 2021, pp. 154–157. https://doi.org/10.1364/OL.412495
[63] "An m by n FLDI Array for Single-Shot Multipoint Disturbance Measurements in High-Speed Flows," *AIAA Scitech 2021 Forum*, AIAA Paper 2021-0599, 2021. https://doi.org/10.2514/6.2021-0599
[64] Shekhtman, D., Hameed, A., Segall, B. A., Dworzanczyk, A. R., and Parziale, N. J., "Initial Shakedown Testing of the Stevens Shock Tunnel," *AIAA Scitech 2022*, AIAA Paper 2022-1402, 2022. https://doi.org/10.2514/6.2022-1402
[65] Goodwin, D. G., "An Open-Source, Extensible Software Suite for CVD Process Simulation," *Proceedings of CVD XVI and EuroCVD Fourteen*, edited by M. Allendorf, F. Maury, and F. Teyssandier, Electrochemical Soc., Pennington, NJ, 2003, pp. 155–162.
[66] Browne, S., Ziegler, J., and Shepherd, J. E., "Numerical Solution Methods for Shock and Detonation Jump Conditions," GALCIT - FM2006-006, 2006.
[67] Segall, B. A., Shekhtman, D., Hameed, A., Chen, J. H., and Parziale, N. J., "Profiles of Streamwise Velocity and Fluctuations in a Hypersonic Turbulent Boundary Layer Using Acetone Tagging Velocimetry," *Experiments in Fluids*, Vol. 64, No. 6, 2023, p. 122. https://doi.org/10.1007/s00348-023-03647-2
[68] *ANSYS Fluent*, Commercial CFD Software, Version 2022, ANSYS Inc., Canonsburg, PA, 2022.
[69] Keyes, F. G., "A Summary of Viscosity and Heat-Conduction Data for He, A, H2, O2, N2, CO, CO2, H2O, and Air," *Transactions of the American Society of Mechanical Engineers*, Vol. 73, No. 5, 1951, pp. 589–595. https://doi.org/10.1115/1.4016339
[70] Dhamankar, N. S., Martha, C. S., Situ, Y., Aikens, K. M., Blaisdell, G. A., Lyrintzis, A. S., and Li, Z., "Digital Filter-Based Turbulent Inflow Generation for Jet Aeroacoustics on Non-Uniform Structured Grids," *52nd Aerospace Sciences Meeting*, AIAA Paper 2014-1401, 2014. https://doi.org/10.2514/6.2014-1401
[71] Roy, D., Schuabb, M., Aultman, M., Duan, L., Segall, B., Keenoy, T., Kokinakos, J., Parziale, N., and Hameed, A., "DNS and Experimental Study of Shock Wave/Turbulent Boundary Layer Interaction over a Mach 6.32 Hollow-Cylinder/Flare," AIAA Paper 2025-3529, July 2025. https://doi.org/10.2514/6.2025-3529
[72] Hameed, A., and Parziale, N. J., "Focused Laser Differential Interferometric Investigation of Turbulent Jet Spectra," *Journal of Spacecraft and Rockets*, Vol. 59, No. 5, 2022, pp. 1565–1573. https://doi.org/10.2514/1.A35292

S. Fu
Associate Editor